

1 Title

2 High-resolution 3D imaging and topological mapping of the lymph node conduit system

3 Authors

4 Inken D. Kelch^{1,2 *}

5 Gib Bogle^{1,3}

6 Gregory B. Sands³

7 Anthony R. J. Phillips^{1,2,4}

8 Ian J. LeGrice^{3,5}

9 P. Rod Dunbar^{1,2}

10 Affiliations

- 11 1. Maurice Wilkins Centre, University of Auckland, Private Bag 92-019, Auckland 1142,
12 New Zealand
- 13 2. School of Biological Sciences, Faculty of Science, University of Auckland, Private Bag
14 92-019, Auckland 1142, New Zealand
- 15 3. Auckland Bioengineering Institute, University of Auckland, Private Bag 92-019,
16 Auckland 1142, New Zealand
- 17 4. Department of Surgery, School of Medicine, Faculty of Medical and Health Sciences,
18 University of Auckland, Private Bag 92-019, Auckland 1142, New Zealand
- 19 5. Department of Physiology, School of Medical Sciences, Faculty of Medical and Health
20 Sciences, University of Auckland, Private Bag 92-019, Auckland 1142, New Zealand

21 Lead contact

22 *Correspondence: Dr Inken D. Kelch, i.kelch@auckland.ac.nz

23 Prof Rod Dunbar, r.dunbar@auckland.ac.nz

24 **Abstract**

25 The conduit network is a hallmark of lymph node microanatomy, but lack of suitable imaging
26 technology has prevented comprehensive investigation of its topology. We employed an
27 extended-volume imaging system to capture the conduit network of an entire murine lymph
28 node ($\approx 280,000$ segments). The extensive 3D images provide a comprehensive overview of the
29 regions supplied by conduits including perivascular sleeves, and distinctive “follicular
30 reservoirs” within B cell follicles, surrounding follicular dendritic cells. A 3D topology map of
31 conduits within the T cell zone showed homogeneous branching, but conduit density was
32 significantly higher in the superficial T cell zone compared to the deep zone, where distances
33 between segments are sufficient for T cells to lose contact with fibroblastic reticular cells. This
34 topological mapping of the conduit anatomy can now aid modeling of its roles in lymph node
35 function, as we demonstrate by simulating T cell motility in the different T cell zones.

36 **Keywords**

37 3D imaging, confocal microscopy, image processing, lymph node, conduit, topology
38 mapping, computer modeling, motility, FDC, follicular reservoir

39 Introduction

40 Sophisticated immune responses are organized within the highly-structured microanatomy of
41 lymph nodes (LNs) where stromal cell networks support the circulation, maintenance, and
42 interaction of highly motile hematopoietic cell types on their continuous quest for cognate
43 antigen (1-3). A key feature of the LN organization is the mesh-like network of fibroblastic
44 reticular cells (FRCs) spanning the LN paracortex, the main homing zone for T cells (4, 5).
45 FRCs organize LN microenvironments and control T cell life in many ways by providing
46 survival signals, aiding migration, and restricting T cell activation (6, 7). They express the
47 chemokines CCL19 and CCL21, important cues for motility, compartmentalization and
48 retention of CCR7-expressing T cells, B cells, and dendritic cells (DCs) (3, 8, 9). In a similar
49 fashion, FRCs appear to be involved in B cell homeostasis, by providing the B cell survival
50 factor BAFF and contributing to CXCL13 expression (10, 11). LN expansion during immune
51 stimulation is mediated by FRCs in synergy with DCs, which can trigger FRC stretching via
52 interaction of CLEC-2 with podoplanin (12, 13). FRC destruction is part of the pathology of
53 several devastating viral diseases, and directly affects the number and functionality of T cells
54 (2, 7, 14). FRC networks also appear in tertiary lymphoid structures at sites of chronic
55 inflammation underlining their central importance to immunobiology (15, 16).

56 Remarkably, FRCs construct a piping system that rapidly conducts incoming lymphatic fluid
57 including tissue-derived antigens across the LN cortex (17-19). This conduit system consists
58 of interconnected ‘micro vessels’ built of a central core of collagen fibers surrounded by a layer
59 of microfibrils and a basement membrane enwrapped by FRCs, and channels molecules < 70
60 kDa from the subcapsular sinus (SCS) to inner LN compartments (17-20). In particular,
61 inflammatory soluble mediators and cytokines can be shuttled directly to high endothelial
62 venules (HEVs), specialized vessels for lymphocyte entry that are surrounded by perivascular
63 “sleeves” formed by FRCs (5, 21-23). Intriguingly, the conduit network persists even if FRCs

64 are temporarily lost, suggesting that it possesses structural integrity, while depending on FRCs
65 for remodeling (10). Many questions remain concerning the heterogeneity of FRC populations,
66 the exact mechanisms by which they regulate immunity, and the advantages of FRC-guided
67 migration of T cells in a 3D space (7, 24). Our understanding of the structure of the conduit
68 network remains limited due to the technical difficulty of capturing these delicate network
69 structures within large tissue volumes (25). Previous approaches to studying the FRC network
70 globally within LNs have relied on *in silico* computer models with pre-defined network
71 properties (26-28), based on information from confocal images on a small scale (29, 30). Large-
72 scale 3D imaging of entire networks has to date been hindered by the limitations of tissue
73 penetration in standard microscopy, and restrictions in resolution of large-scale imaging
74 techniques (31, 32). An additional complexity is that moving from small-scale measurements
75 in 2D to large-scale measurements in 3D requires specialized non-trivial algorithms that often
76 require custom computation by the operating lab to fit a particular purpose (32).

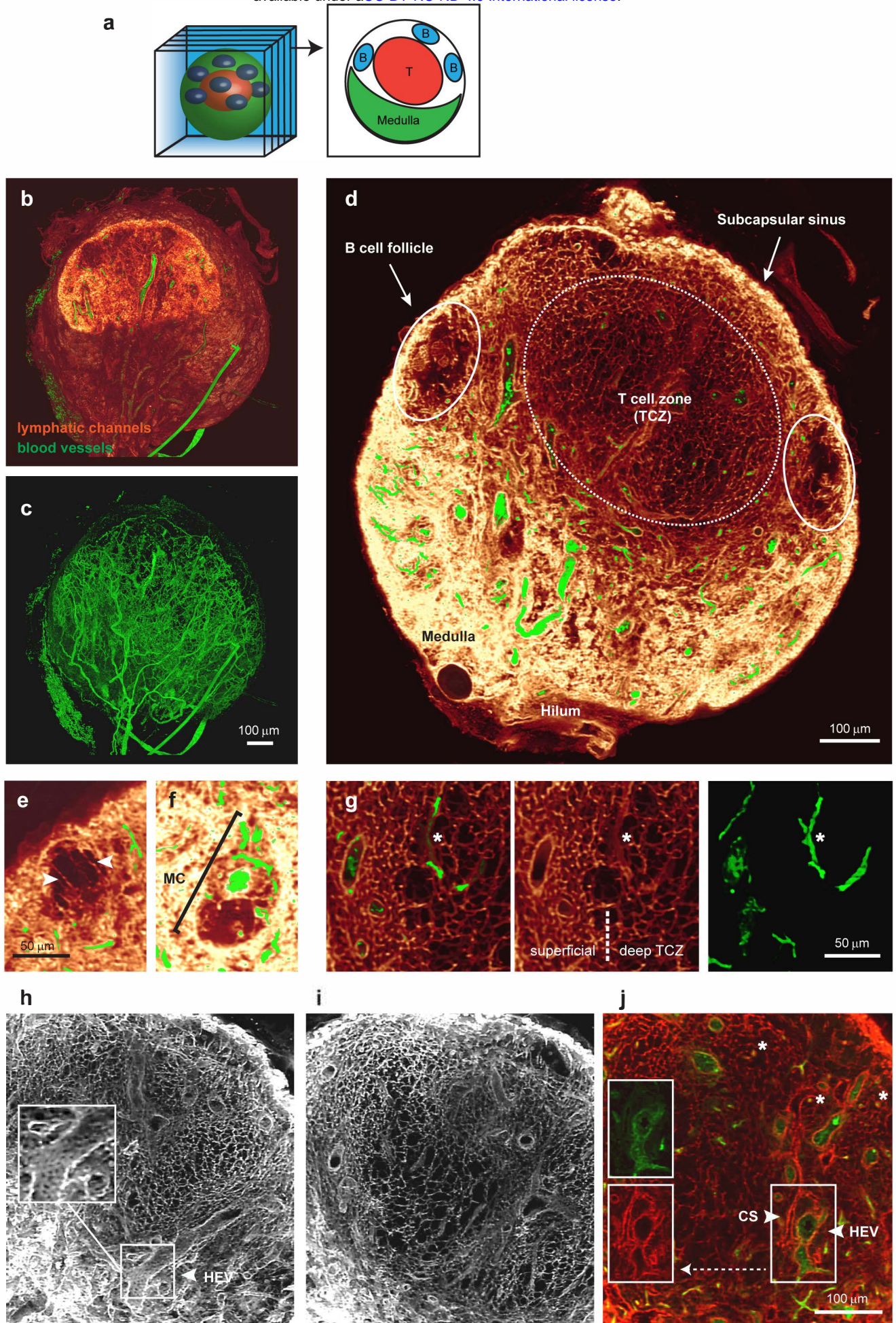
77 To provide a comprehensive picture of the LN conduit network we used a unique confocal
78 block-face imaging system referred to as EVIS (extended-volume imaging system) (33, 34)
79 and captured the conduit and blood vessel system of an entire murine LN. From the obtained
80 seamless 3D images, we extracted a continuous topology map of the conduits in the T cell zone
81 (TCZ) and quantified the network structure with the help of custom image processing tools.
82 The obtained topology map permitted the assessment of 3D network parameters at
83 unprecedented scale and served as a realistic template for *in silico* simulations of T cell motility.
84 Our measurements revealed significant differences in conduit segment density between the
85 deep and superficial TCZs, making it likely that T cells in the deep zone lose contact with the
86 FRC network more frequently. We were surprised to find distinctive tracer accumulations in
87 the B cell follicles, and we visualized the intriguing organization of the conduit-supplied spaces
88 surrounding FDCs with new clarity. Our topology map provides a unique reality-based road

89 map of the intricate 3D organization of the LN conduits that can be incorporated into the
90 increasingly sophisticated theoretical models seeking to understand and predict complex
91 immune processes within LNs (35).

92 Results

93 *Extensive 3D imagery permits volume views of the continuous conduit network*

94 Previously, studies of the LN conduit system have relied on microscopic images with limited
95 depth information. By performing EVIS imaging at a voxel resolution of 1 μm we were able
96 to capture a popliteal LN sized 850 x 750 x 900 μm in its entirety. Organ-wide anterograde
97 labelling of the lymphatics and blood vessels was achieved by injecting wheat germ agglutinin
98 (WGA) conjugated to different fluorophores into the footpad and the supplying blood vessel,
99 respectively. The resulting 3D image permits detailed insights into the overall LN anatomy
100 (Fig 1). As a 38kDa molecular tracer, WGA recapitulates the routes of lymph-borne molecules
101 <70kDa through the LN. Strong WGA-labelling can be seen in the SCS and the medulla,
102 thereby fully enclosing the LN. By virtually cropping the 3D volume (Fig 1 a), views of the
103 interior organization (Fig 1 b) and the dense network of blood vessels running through the LN
104 are revealed (Fig 1 c). The conduit network is most structured in the central TCZ (Fig 1 d), and
105 is sparse in the B cell follicles, with only a few channels running beside any one follicle (Fig 1
106 e). The medulla is richly filled with WGA, providing a high staining intensity in the lymphatic
107 sinuses, yet medullary cords, strands of parenchymal tissue that extend into the medullary space
108 and are densely packed with cells (5, 36), are clearly distinguishable and contain at least one
109 central blood vessel (Fig 1 f).



110 Fig 1. Detailed 3D images of the conduit network in a whole LN.

111 EVIS imaging of an entire popliteal LN generated a 3D volume image of which interior
112 slices can be viewed individually (**a**). 3D image reconstruction of the entire LN shows
113 (**b**) lymphatic channels filled with the tracer molecule WGA (red glow) together with
114 dextran-labelled blood vessels (green), or the blood vasculature alone (**c**). An interior
115 view of 20 μm thick optical sections (**d - i**) and a 1 μm slice (**j**) permits detailed insights
116 into the LN architecture. A cross-section of the LN displays the location of cell-specific
117 zones (**d**), while close-ups reveal anatomical details including the arrangement of long
118 conduits descending from the SCS at the edges of a B cell follicle (arrowheads, **e**), a
119 medullary cord (MC) with a central blood vessel situated amongst the WGA-filled
120 sinuses of the medulla (**f**), and the transition from dense to sparse conduit networks in
121 the superficial to the deep TCZ (**g**). The conduit network forms a highly organized grid
122 within the TCZ (white, **h, i**; red, **j**) interspersed with cortical sinuses (CS, arrowhead,
123 **j**) and blood vessels (green) including HEVs, which are closely surrounded by cells
124 displaying a cobblestone-like morphology (arrowhead, **h, j**). Besides larger blood
125 vessels, small blood vessels are frequently enclosed by conduits (asterisks, **g, j**).
126 Image rendering was performed in VoxX (**a - i**) and ImageJ (**j**). See also [S1 Fig](#), [S1](#)
127 [Video](#), and [S2 Video](#).

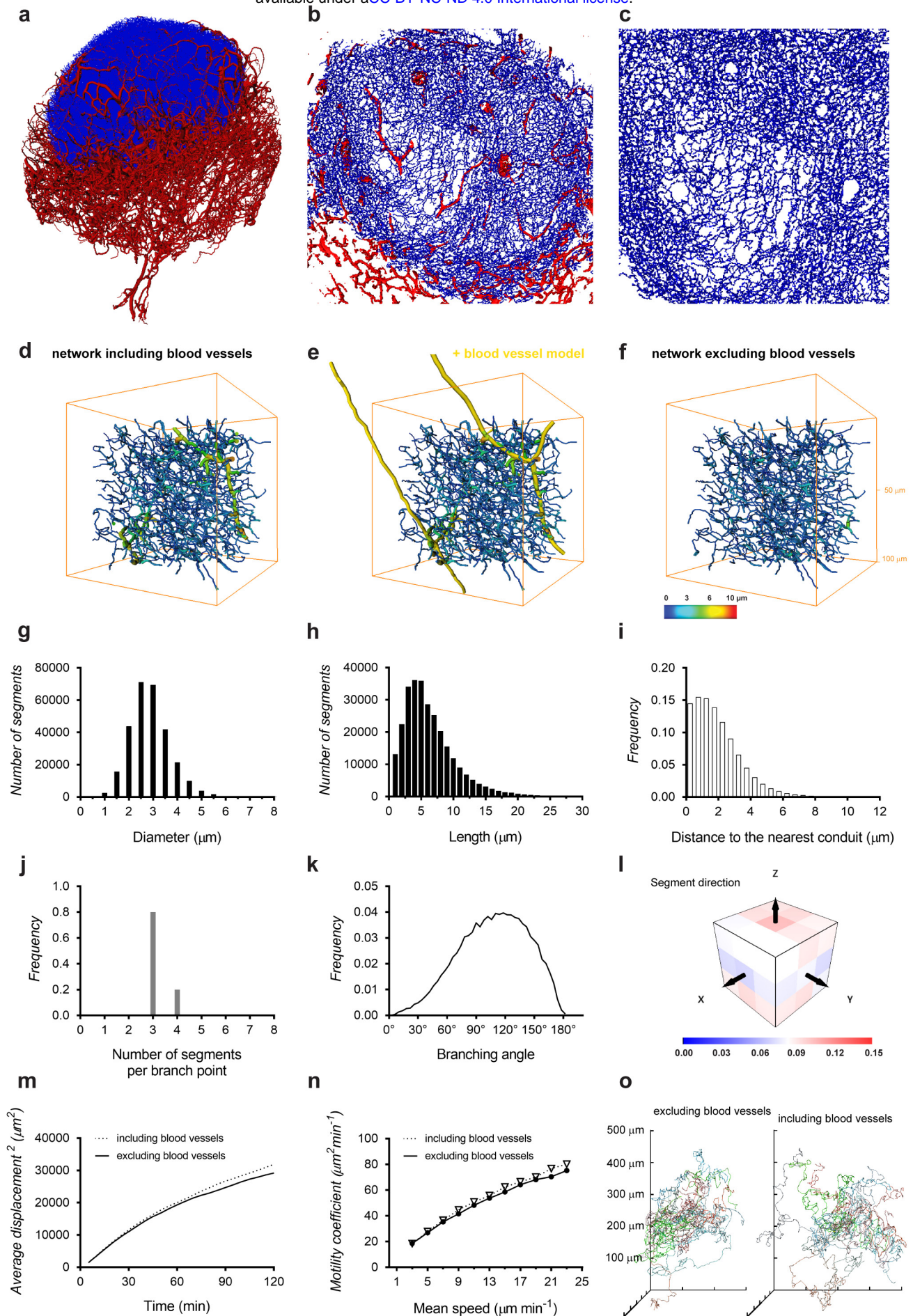
128 Within the TCZ the conduit network appears most dense in the superficial and interfollicular
129 zones, while a sparser network structure becomes apparent within its center ([Fig 1 d, g-j](#)),
130 consistent with previous definitions distinguishing the deep TCZ from surrounding regions
131 (37). Particularly strong staining could also be observed around HEVs and smaller blood
132 vessels, which both appear surrounded by a sleeve contiguous with the conduit network ([Fig 1](#)
133 [g-j](#)). However, intraluminal staining of blood vessels with lymph-derived WGA was not
134 observed ([Fig 1 g-j](#), [S2 Fig](#)). Cortical sinuses (38) also display strong labelling, but can be

135 distinguished from blood vessels by lack of blood vessel-specific WGA-staining (Fig 1 j) and
136 their continuity with the medullary sinuses, a feature that becomes evident in animations of the
137 3D dataset (S1 and S2 Video). Interestingly, while it was previously reported that conduits are
138 primarily focused on HEVs, we observed in our 3D images that conduits frequently terminate
139 on cortical sinuses, which are often located in close proximity to blood vessels (S1 Fig).
140 Examining tissue sections using conventional immunofluorescence microscopy confirmed that
141 conduits connect to cortical sinuses made up of LYVE-1+ lymphatic endothelial cells (S1 Fig).
142 Together, these images demonstrate that the conduit system connects the SCS with cortical
143 sinuses that drain into the medulla, as well as the perivascular sleeves surrounding blood
144 vessels including HEVs, thereby providing a continuous piping system for incoming lymphatic
145 fluid (S1 and S2 Video).

146 *Quantification of the conduit network topology*

147 The availability of an extensive 3D volume image of the continuous LN conduit network
148 permits quantification of its network statistics at unprecedented scale and provides an exciting
149 opportunity for the realistic modeling of T cell motility. We previously imaged and quantified
150 the blood vessel system of a mesenteric LN using a set of custom-developed image processing
151 and analysis tools (33), and now applied these tools to perform large-scale 3D analysis on the
152 conduit network. The image processing consists of a number of steps including thresholding
153 and skeletonization, which transform the pixel-based image data into a 3D topology map. The
154 topology map describes the network as a system of connected tubes and enables a direct read-
155 out of network parameters (Fig 2). In order to study the network topology of the conduit system
156 in the central paracortical TCZ and its implications for T cell biology, the extraction procedure
157 was optimized to best capture the network in this region (Fig 2 a-c). A limitation of this process
158 was posed by the occurrence of continuous tracer-labeled spaces fully enclosing large blood
159 vessels, such as HEVs (S2 Fig, S3 Video), identified previously as perivascular sleeves (5).

160 This feature of the conduit network provided an obstacle for the skeletonization process (S3
161 Fig) and required us to adapt our image processing strategy. We overcame this problem by
162 utilizing the co-stained blood vessels and subtracting the segmented blood vessel image data
163 from the conduit image. In our previous study (33), we found blood vessels in the LN typically
164 have diameters between 4 and 87 μm , while diameters of conduits are reported to lie in the
165 range of 1 to 2 μm (17, 19, 20, 39). By removing the blood vasculature from the conduit data,
166 vessels of the size of blood vessels could be effectively excluded (Fig 2 d-f). The resulting
167 ‘clean’ conduit network contained 282,716 segments with a mean diameter of 2.9 μm and an
168 average length of 6.5 μm (Fig 2 g, h; Fig 3 h, i). Within the TCZ conduit network, spanning a
169 volume of about 0.079 mm^3 , the conduit segments had a combined length of 1.84 m and a
170 density of $3.54 \cdot 10^6$ segments mm^{-3} (Fig 3 f, j). To obtain a measure of spacing in the network,
171 we applied an algorithm that measures the distance to the nearest conduit segment starting from
172 a regular fine grid of points located in the LN volume (33). This calculation revealed that the
173 majority of locations in the LN TCZ lie within a very short distance of the nearest conduit (<
174 4 μm , 90.9%) (Fig 2 i). Overall, the conduit network displayed an even branching pattern, with
175 the majority of branching points representing bifurcations and branching angles centered
176 around 120° (Fig 2 j, k). The segment orientation had no observable bias in direction (Fig 2 l).



177 Fig 2. Network topology of the LN conduits in the TCZ.

178 Deploying custom-developed image-processing tools, a description of the conduit
179 network in terms of nodes and links was generated from the 3D image data and used
180 to estimate network parameters. 3D projections of the blood vasculature (red) and the
181 conduit network in the TCZ (blue) as a whole (**a**) and magnified views of the TCZ (**b**,
182 **c**) expose the complexity and the high level of detail in this dataset. The full conduit
183 data includes large segments with diameters over 5 μm (**d**), but these represent blood
184 vessels as the overlay with the blood vessel model (yellow) indicates (**e**). A blood
185 vessel-free conduit network (**f**) was obtained by removing the majority of blood vessels
186 from the 3D image prior to the network extraction in a semi-automated process. This
187 TCZ conduit network excluding blood vessels was employed to calculate the
188 distribution of segment diameters (**g**), lengths (**h**), the branching pattern (**j**), branching
189 angles (**k**), and segment orientation (**l**), while the full dataset including blood vessels
190 was used to calculate the minimum distance to the nearest conduit (**i**). Simulation of T
191 cell motility utilizing these conduit data provides the cell displacement at a mean speed
192 of 13 $\mu\text{m min}^{-1}$ (**m**), motility coefficients for different speeds (**n**), and a spider-plot
193 representation of migration paths in a network with and without blood vessels (**o**). See
194 also [S2 Fig](#), [S3 Fig](#) and [S3 Video](#).

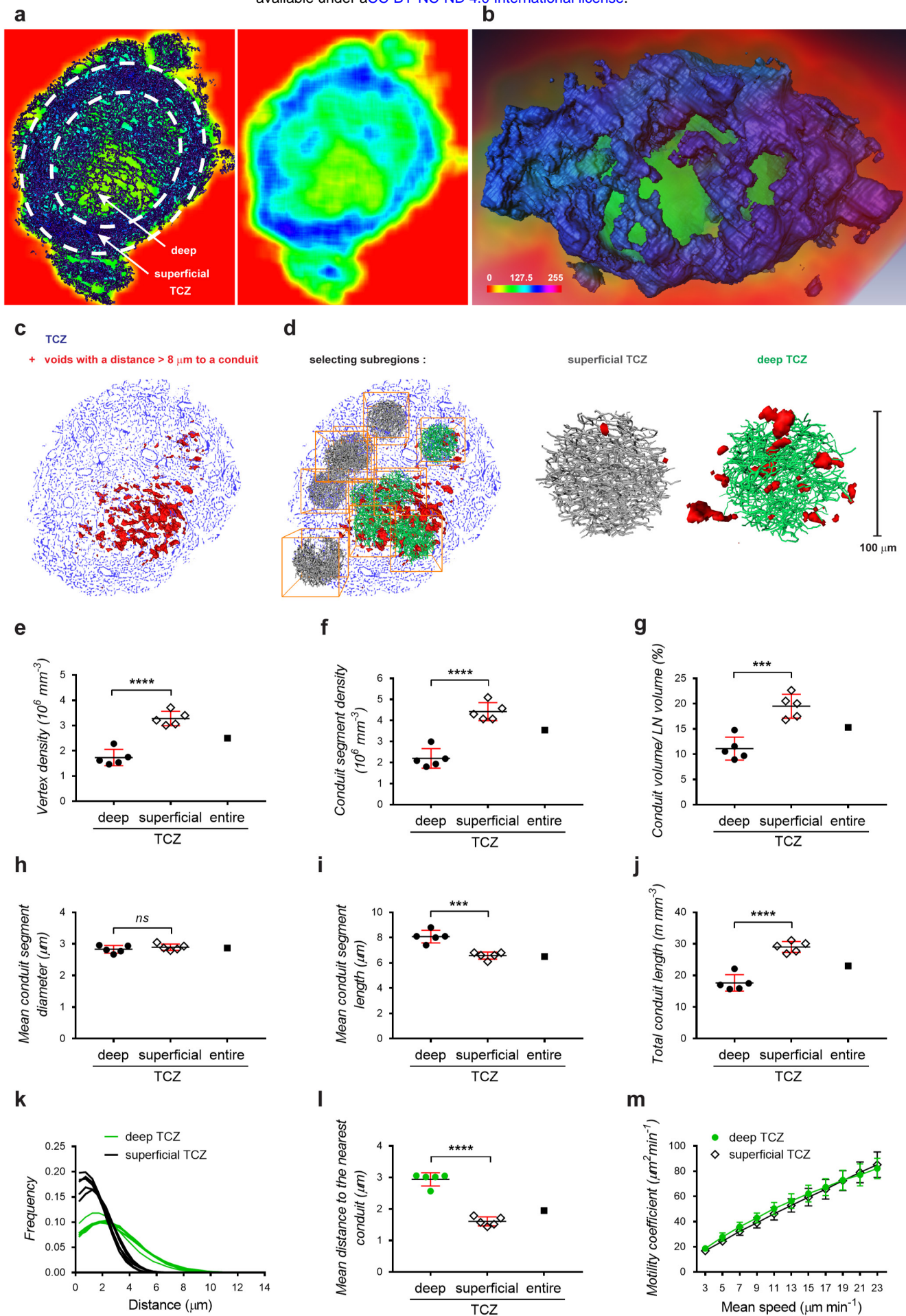
195 We then tested how this network topology would predict the migration of T cells in 3D, when
196 stimulated T cells are restricted to migrating along the network segments, as if in continuous
197 contact with FRCs. We simulated the paths of a large number of cells on the extracted conduit
198 network to calculate the coefficient of motility (C_m) as an index of dispersal rate in 3D space,
199 representing the rate at which T cells can scan a volume of paracortex for the presence of
200 cognate antigen. In these simulations, we used values of mean speed in the range typically
201 measured by intra-vital microscopy (40-44). The average displacement of cells ([Fig 2 m](#)) at

202 T=60 min was used to calculate C_m , (Fig 2 n), and the correlation we generated between mean
203 speed and C_m was broadly consistent with values previously measured *in vivo* (41). The average
204 displacement and the corresponding C_m values are not significantly increased when blood
205 vessels are included in the analysis (Fig 2 m, n), but cell tracks show a slight variation due to
206 the availability of the blood vessels and the sheaths that often surround them as additional
207 migration paths (Fig 2 o).

208 *Topology differences in the deep and superficial TCZ*

209 It was evident in the 3D conduit image and the topology map that the conduit network in the
210 TCZ is not homogeneous, but displays different densities in the superficial and deep zone
211 (Fig 3), concordant with previous descriptions (37). After coloring regions based on their
212 segment density, it is possible to visually distinguish the deep TCZ, containing a rather open
213 mesh, from the superficial zone, which is characterized by a dense network of conduits and
214 fully encloses the spherical central T cell region (Fig 3 a, b). In a different approach to
215 visualizing the variable spacing in the network, distances to the nearest conduit segment were
216 measured in 3D and locations further than 8 μm from any conduit were displayed in red
217 (Fig 3 c, d). An accumulation of red voids is located centrally in the deep TCZ, while they were
218 absent from superficial locations. To quantify these regional differences, 5 spherical subregions
219 with a diameter of 100 μm were selected from the superficial and deep TCZ each and examined
220 using the topology toolset (Fig 3 d). The deep TCZ contained significantly fewer vertices,
221 segments, and a smaller conduit volume per region than the superficial zone, confirming
222 visually observable differences in conduit density (Fig 3 e-g). While the conduit diameters in
223 both locations showed no measurable difference, individual segment lengths were considerably
224 shorter in the superficial zone, yet the combined conduit length of all segments was longer than
225 in the deep TCZ (Fig 3 h-j). In summary, the deep TCZ can be perceived as a stretched version

226 of the conduit network in superficial areas. As a result, cells in the deep TCZ have a 50%
227 greater mean distance to the nearest conduit segment (Fig 3 l), reaching distances well beyond
228 the cell diameter of a murine lymphocyte (2.5-3 μm) (45), and making it unlikely that cells in
229 this region are in contact with a conduit segment at all times. In contrast, distances measured
230 in the superficial zone would allow nearly continuous contact with the network (conduit
231 distance < 4 μm : 73.4% in the deep TCZ vs. 96.8% in the superficial TCZ; conduit distance <
232 6 μm : 92.2% deep vs. 99.9% superficial) (Fig 3 k).



233 Fig 3. Comparison of conduit network parameters in the deep and superficial TCZ.

234 Differences in conduit density between the deep and superficial TCZ can be visualized
235 by averaging and color-coding pixel densities over small image volumes in a ‘moving
236 average’ display, shown as a rainbow spectrum (**a, b**). A cross-section of the moving
237 average display exposes how dense regions in the periphery of the LN (blue) surround
238 an inner region of lower conduit density (green), directly representing dense or sparse
239 occurrence of conduit segments in the corresponding section of the conduit network
240 image (dark blue, left panel), respectively (**a**). Volume rendering (**b**) of the entire TCZ
241 using this approach shows the dense superficial zone (blue) enclosing a central region
242 of sparse conduits (green). Alternatively, the TCZ conduit map was employed for
243 calculating the distances to the nearest conduit and voids with a distance of over 8 μm
244 were displayed in red, indicating larger distances within the deep TCZ as opposed to
245 outer regions (**c**). From these two zones 10 subregions were selected for comparative
246 analysis (**d**); including the number of vertices (**e**), the number of conduit segments (**f**),
247 the conduit volume (**g**), conduit segment diameters (**h**), conduit segment lengths (**i**),
248 and the combined conduit length (**j**). The distributions of the minimum distances to the
249 nearest conduit (**k**) and the average minimum distance (**l**) further exemplify the larger
250 spacing within the deep TCZ. Simulation of T cell motility predicts similar motility
251 coefficients within the deep TCZ and the surrounding superficial zone (**m**). Data are
252 from one experiment (each point represents one 100 μm subregion, N = 10) and plots
253 show means \pm SD. **** p < 0.0001, *** p < 0.001, ns = not significant, Student’s t-test.
254 See also [S4 Fig](#).

255 We then used our simulations of T cell migration to predict motility coefficients separately in
256 the superficial and deep zones, assuming that T cells remained in contact with the conduit
257 network. The calculated 3D motility coefficients gradually increased with the speed of

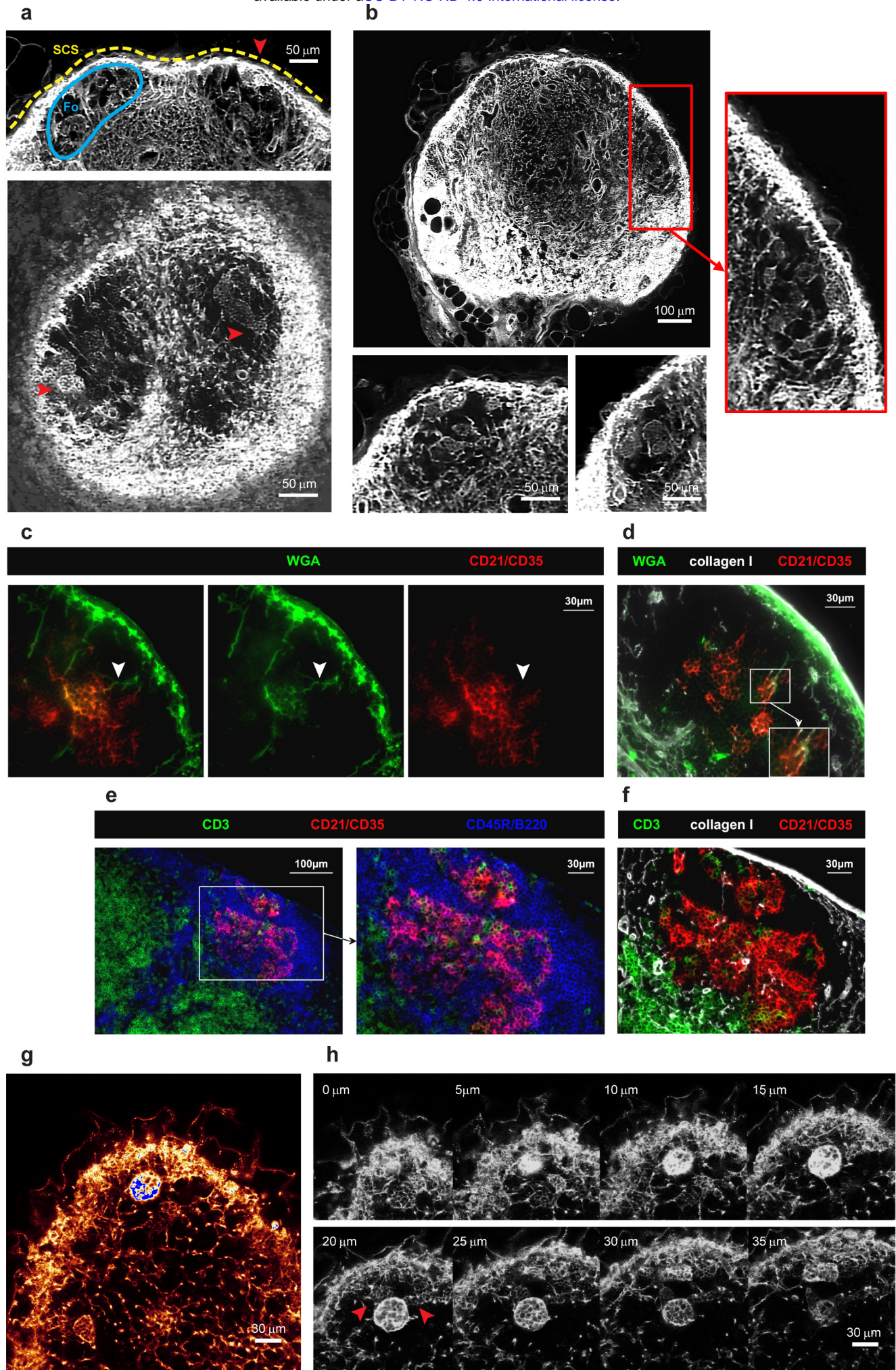
258 migration but there were no significant differences in motility coefficients between the zones
259 (Fig 3 m).

260 With respect to potential specialised immune functions within the different TCZs, we noted
261 differences in the distribution of proliferating T cells in 2D sections of resting LNs. Ki-67+
262 proliferating cells were often found in close proximity to the conduit network, and seemed
263 more frequent in the peripheral TCZ than the deep T cells zone (S4 Fig), reinforcing the
264 possibility that close cell contact (or the cues they provide) is important for T cells in the
265 superficial TCZ.

266 *Conduit organization in B cell follicles*

267 EVIS imaging of WGA-perfused LNs led to the unexpected observation of distinctive tracer
268 accumulations inside B cell follicles. Compared to the dense conduit network in the TCZs,
269 conduits are very rare in the B cell zones (Fig 4 a, b), although a small number of conduits
270 could often be visualized descending directly from the SCS, consistent with channels
271 previously referred to as follicular conduits (39). However, unexpectedly we also observed
272 distinctive WGA tracer accumulations within the B cell regions, appearing as discrete
273 multilobular spaces reminiscent of ‘honeycombs’ that are connected to the SCS and each other
274 via follicular conduits (Fig 4 a, b, S4 Video), occasionally aggregating into larger contiguous
275 cavities. Hence these clusters appear as striking dense accumulations of WGA tracer within B
276 cell zones that are otherwise relatively devoid of conduits (Fig 4 g, h). To test how these WGA-
277 filled spaces relate to the location of follicular dendritic cells (FDCs), we used multicolor
278 immunohistochemistry to identify FDCs in WGA-perfused LNs. The FDC marker
279 CD21/CD35 co-localized with the observed deposits of WGA tracer (Fig 4 c), confirming that
280 the spaces we visualized surrounded and intercalated with FDCs deep within B cell follicles.
281 Additional stains using collagen I to visualize conduit channels confirmed the transport of

282 WGA through follicular conduits and deposition of WGA on FDCs (Fig 4 d). Moreover, the
283 arrangement and morphology of FDCs within the B cell follicle, as shown by co-staining with
284 collagen I and a B cell marker, closely mirrors the location of the spaces typically filled by
285 WGA (Fig 4 e, f). High-resolution confocal image stacks revealed some diversity in the spaces
286 where the WGA tracer accumulated within the follicles (Fig 4 g, h, S5 Video). As well as the
287 almost spherical structures of ~30 μm diameter that were brightly labeled, we noted weaker
288 WGA tracer accumulation in adjacent honeycombed regions (Fig 4 h, arrows), consistent with
289 the various shapes of FDC clusters (Fig 4 e, f). We also noted that the WGA signal inside B
290 cell follicles was not as abundant in the 2D frozen sections (Fig 4 c, d) compared with our 3D
291 data (Fig 4 a, b, g, h), suggesting that tracer may be washed off during frozen section
292 preparation while being retained in the PFA-fixed and resin-embedded LNs we used for 3D
293 imaging.



294 Fig 4. The follicular conduit.

295 3D EVIS images of a popliteal LN with WGA-labelled conduit paths contain brightly
296 labelled multilobular spaces (red arrowheads) within the otherwise unstained B cell
297 follicles (Fo) underneath the SCS that can be repeatedly seen in 3D projections of 20
298 μm thickness (**a**) and 2D image slices (**b**). In immuno-labelled tissue sections of WGA-
299 perfused inguinal LNs, WGA (green) is found in follicular conduits descending from
300 the SCS (white arrowheads) connecting to cellular clusters expressing the FDC-
301 marker CD21/CD35 (**c, d**). The morphology and location of WGA-labelled cell clusters
302 within B cell follicles (**d**) are generally consistent with the anatomy of FDCs in these
303 regions (**e, f**) as co-staining with markers for B cells (CD45R/B220), T cells (CD3), and
304 collagen I confirms. High-resolution confocal images (with a voxel resolution of 0.36 x
305 0.36 x 1 μm) of a WGA-perfused popliteal LN provide insights into the staining pattern
306 within and around the WGA accumulations (**g**), and show a particularly bright cluster
307 in several z steps (**h**) directly neighboring spaces with weaker labelling (red
308 arrowheads). Images are representative of at least 6 LNs (from N = 5 mice) in which
309 multilobular cell clusters could be observed. See also [S4 Video](#) and [S5 Video](#).

310 Discussion

311 We set out to map the conduit network across an entire LN to enable measurements of its
312 topology. Here we present extensive 3D imagery of the conduit channel system of a whole LN,
313 permitting detailed insights into the conduit organization and its connectivity with blood and
314 lymphatic vessels. We also provide a continuous reality-based computer representation of the
315 TCZ conduits to enable large-scale quantification and downstream use in computer models of
316 immune processes.

317 The conduit system has an intricate spatial relationship with the blood vessels and the
318 lymphatic sinuses. Besides stabilizing the organ structure through their scaffold-like
319 organization, conduits are thought to provide a short cut between incoming lymph and HEVs
320 (18, 19). Although there is evidence that some molecules such as chemokines can gain access
321 to the HEV lumen through the conduit network (18, 19, 22), this may depend on transport
322 through endothelial cells by transcytosis (46). We did not observe significant intra-vascular
323 staining with WGA supplied into the conduits, implying that this 38 kDa molecule did not
324 readily have access to the vascular lumen but was instead retained in a perivascular sleeve. Our
325 3D imagery therefore supports the concept that conduit segments descend from the SCS,
326 branch through the paracortex, and richly supply perivascular sleeves including those
327 surrounding HEVs. Notably, these perivascular sleeves represent the first space encountered
328 by cells exiting the bloodstream, and suggest an under-explored role for the conduits, in
329 conveying molecules directly from the SCS to lymphocytes and antigen-presenting cells that
330 have just entered the LN from the blood. These data also lead us to conclude that these regions
331 do not represent major sites of lymph drainage into the vasculature. Instead, we observed
332 conduits frequently terminating in lymphatic sinuses that are blind-ended invaginations of the
333 medullary sinuses, which is likely to provide the necessary outlet for accumulating lymph and
334 potentially aids cell egress at these locations (47).

335 Analysis of over 280,000 conduit segments in the 3D topological model we generated revealed
336 a homogeneous branching pattern, with bifurcations being the most prevalent branching
337 structure and no more than 7 segments meeting at any one point. The level of connectivity that
338 we measured between neighboring nodes is slightly lower than that measured by Novkovic,
339 Onder (30), who note the presence of highly connected nodes with more than 12 edges, based
340 on confocal images of CCL19-expressing cells across a small fraction of the paracortex. The
341 data presented here represent network parameters from an entire TCZ providing a clear
342 advantage to previous extrapolations from small LN regions. In contrast to their cell-based
343 graph network, our conduit model provides a road map of the collagen-bearing conduit
344 channels that the FRCs ensheath, including their exact lengths and orientation. It is possible
345 that two or more conduit branch points in our model fall within the area of one cell body, to
346 account for some of the differences in network topology, yet our data do not support the
347 prevalence of highly connected nodes as they report. New opportunities are now likely to arise
348 by combining the techniques we developed with those established for imaging FRC cell bodies,
349 for example to track the structure of entire conduit networks in response to immune stimuli or
350 disturbance of FRC network integrity, phenomena that have only recently begun to be explored
351 (10, 13, 14, 30).

352 A striking feature that is visually obvious in our 3D images is the variation in conduit network
353 density between the deep and superficial T cell regions. The topology map of the TCZ conduits
354 we generated allowed us to quantify significant differences in conduit segment density,
355 segment length, and inter-segment gap size between both zones. Our 3D imaging data are
356 therefore consistent with several studies that previously identified a structural inhomogeneity
357 within the TCZ in the LN paracortex. While the deep zone has been described as loosely
358 interspersed with a network of FRCs and conduits, the peripheral zone was noted to contain a
359 much denser mesh and a higher abundance of HEVs (37). The superficial TCZ (48) has also

360 been referred to as the cortical ridge (37, 49), or the peripheral T cell region (50), and is
361 continuous with the interfollicular regions between the B cell follicles closer to the SCS (51,
362 52). Although the biological significance of this structural segregation is still unclear,
363 independent reports have pointed to an asymmetry in cell positioning in both zones. Naïve T
364 cells tend to occupy the deep TCZ, whereas memory T cells preferentially locate to the
365 superficial zones, and innate effector cells can often be found in the interfollicular regions (37,
366 53, 54). Similarly, subtypes of resident and migratory DCs seem to preferentially locate to
367 either the deep, the superficial, the interfollicular zones, or regions close to the medulla (49,
368 50, 55). It has also been frequently observed that following immune challenge T cells cluster
369 in peripheral regions or locations close to the medulla (50, 51, 56-58). It is therefore intriguing
370 to note that Ki67-expressing cells in the resting LNs we examined were often located in very
371 close proximity to a conduit, and tended to localize to the periphery of the TCZs (S4 Fig). IL7-
372 production may be higher in the peripheral TCZ (59), and close proximity to the FRC network
373 might increase access to homeostatic survival and growth factors for memory or recently-
374 primed T cells.

375 Our measurements of conduit density in the deep and superficial TCZs led us to conclude that
376 while T cells within the superficial zone could remain in almost continuous contact with FRCs
377 wrapped around the conduits, the larger gap size in the deep T cells zone does not guarantee
378 simultaneous contact for all T cells in this region. While *in vivo* imaging studies suggested that
379 T cell motility is generally bound to the FRC network (43, 60), T cells were observed to
380 occasionally leave the FRC paths and migrate perpendicular to the FRC scaffold. Recent data
381 established that T cells migrate in a sliding manner on the FRC network and suggest that fast
382 scanning rates are achieved through low adhesiveness to the FRC substrate (43, 61). Our 3D
383 data confirm that a dense continuous network is present to support the migration of cells across
384 the TCZ, but the more open topology in the deep TCZ substantially increases the likelihood of

385 an occasional loss of contact. Interestingly, theoretical studies of the FRC network have
386 concluded that the odds of a cognate T/DC encounter are in fact not significantly increased by
387 confining migration to a network (25-28).

388 When we used our 3D topology map of the conduit network as pathways to simulate FRC-
389 bound T cell migration, we observed an increase in the coefficient of motility as velocities
390 increased across the range commonly measured *in vivo* (40, 41), confirming that higher
391 velocities translate to faster scanning rates. However in these simulations, where T cell
392 migration was solely restricted to the paths represented by the conduit network, we could not
393 detect substantial differences in the coefficients of motility between the deep and superficial
394 TCZs at any particular velocity. This may relate to the fact that although the density of the
395 conduit networks differs in these two zones, their branching topology is very similar, with the
396 network in the deep zone effectively representing a “stretched” version of that in the superficial
397 zone. Some previous *in vivo* measurements recorded higher T cell velocities in the deep TCZ
398 compared to peripheral zones, which implies that motility coefficients could differ accordingly
399 in these regions *in vivo* (44, 62). Future models of T cell migration will now be able to
400 incorporate our measurements of conduit network topology to model the conduit/FRC-guided
401 component of T cell motility, as we have shown here. However, accurate models will benefit
402 from incorporating additional factors, including the effect of chemokinesis and chemotaxis
403 (63) especially driven by CCL19 and CCL21 (3, 57); the need for T cells to migrate around
404 obstacles (26) including each other (64); and binding to DCs (44), as well as external factors
405 such as confinement affecting the mode of cell migration (43, 61).

406 In summary, our data provide quantitative support for the concept that the FRC and conduit
407 network in the paracortex are arranged in a way that supports different processes in spatially
408 distinct functional zones.

409 In the B cell follicles, conduits have previously been found similar in diameter and particle size
410 exclusion (molecules >70 kDa) to those in the TCZs, although they don't span the B cell follicle
411 but descend as sparse short parallel channels from the SCS to converge with FDCs in the center
412 of the follicle (39). Here we confirm this topology of the follicular conduits, but we also show
413 that they supply a space surrounding the FDCs, that we propose be termed "follicular
414 reservoirs". These honeycombed spaces surrounding FDCs are remarkably well defined and
415 can easily be distinguished in 3D images from the voids of unstained cells surrounding them
416 in the follicles. While these structures could be easily identified in all PFA-fixed and LR white-
417 embedded preparations of whole LNs, staining was frequently lost in acetone-fixed
418 cryosections, suggesting that the fluorescent tracer is in soluble, unbound form within the
419 follicular reservoirs. This phenomenon may also explain why these structures have not been
420 seen in this clarity in previous studies. Our methods to label and preserve the material within
421 the follicular reservoirs open the way for future studies to identify all the cell populations
422 involved in their formation, to clarify the mechanisms by which molecules from the SCS
423 accumulate within them, and to track the changes they undergo during immune activation and
424 germinal center formation.

425 The identification of follicular reservoirs supplied directly by fluid from the SCS is important
426 when considering the supply of antigen to B cells (39, 65). While free diffusion limits the speed
427 at which soluble antigen can reach the deeper follicular region from the SCS, the follicular
428 conduit allows these materials to be rapidly channeled directly to B cells and FDCs in the center
429 of the follicle, which have been shown to readily take up small non-complexed molecules (66,
430 67). In the presence of local Ig or small complement molecules soluble antigen could then be
431 complexed and retained by FDCs to fulfill the prerequisite for sustained B cell activation (66,
432 68). We suggest that the follicular reservoirs we have identified are likely to play a pivotal role
433 in this process. In addition, the follicular conduits may enable FDCs to access signaling

434 molecules < 70kDa delivered from incoming lymphatic fluid or cells near the SCS, in order to
435 respond rapidly and directly to external stimuli.

436 It is important to note that the precise roles of the conduit system in distributing molecules to
437 different LN compartments remain unclear. Several groups reported that DCs and B cells can
438 obtain antigen directly from the conduits, providing a fast antigen delivery system that extends
439 deeply within the LN (19, 20, 67, 69). However, Gerner, Casey (50) have challenged this
440 prevailing view, concluding that antigen dispersal to DCs and subsequent T cell stimulation is
441 dominated by conduit-independent diffusion. Instead the conduit system may simply enable
442 equilibration of fluid, with a subsidiary role in transporting signaling molecules (50). Thierry,
443 Kuka (70) recently provided additional support for the conduit system acting as a drainage
444 system that allows IgM produced in the parenchyma to readily exit the LN and assure a rapid
445 response to infection. Specifically localizing these different immune processes with respect to
446 the spatial variations in the conduit network will help improve our ability to control and
447 manipulate immune responses (50, 71).

448 In summary, the data reported here present the first reality-based description of the conduit
449 network across an entire murine LN paracortex. The extracted topology network provides a
450 useful substrate for theoretical models of LN biology (35), such as 3D motility models and
451 models of fluid distribution (29), as well as providing new insight into the structure of a
452 network that is crucial to many immune functions.

453 **Materials and Methods**

454 **Mice**

455 All animal work was performed in accordance with the guidelines and the requirements of the
456 New Zealand Animal Welfare Act (1999) and approved by the University of Auckland's
457 Animal Ethics Committee. C57BL/6J mice were purchased from The Jackson Laboratory.
458 Experimental protocols employ 9-22 weeks old male C57BL/6J mice housed in the
459 conventional animal facility unit at the School of Biological Sciences at the University of
460 Auckland under environmentally controlled conditions (temperature and humidity) and a
461 12:12-h light/dark cycle. Animals were group-caged in transparent IVC cages with wood-chip
462 bedding and environmental enrichment, in close proximity to other cages so that auditory,
463 visual and olfactory stimulation was present. We assessed animals daily for health and welfare,
464 and access to food and water.

465 **Tissue preparation for EVIS imaging**

466 For *in vivo* staining of murine LNs we used Alexa Fluor 488, 555, TMR or 647 conjugated
467 WGA (wheat germ agglutinin, Invitrogen), TMR-conjugated 2000 kDa dextran (Invitrogen)
468 and anti-LYVE-1 antibody (R&D Systems) that was fluorescently conjugated using the Alexa
469 Fluor 488 Antibody Labelling Kit (Invitrogen). For the labelling of LN conduit paths
470 fluorescently conjugated WGA was used as an anterograde tracer. After brief anesthesia, 50 μ l
471 of WGA-Alexa Fluor 488 (1mg/ml) were injected into the footpad of C57BL/6 mice and let to
472 circulate for 30-60 minutes. This was followed by labelling the blood vascular system using a
473 sequence of 1 ml fluorescent WGA-TMR (50 μ g/ml at 20 μ l/min) and 1 ml 2000 kDa dextran-
474 TMR (500 μ g/ml, Invitrogen)/2.5% gelatin mix (at 50 μ l/min) in a post mortem local perfusion
475 technique as described earlier (33). Excised popliteal LNs were fixed in 4% PFA, 3% sucrose

476 at 4°C overnight before embedding in stable resin for EVIS imaging. Resin embedding was
477 carried out by first dehydrating the tissue and infiltrating with LR white (hard grade,
478 ProSciTech) followed by curing for 6 hours at 60°C as previously described (33). The
479 observable tissue shrinkage that occurs during this process was estimated to be 20%.

480 **Tissue staining and conventional confocal microscopy**

481 To achieve triple staining of the blood vasculature, conduit channels, and lymphatic vessels in
482 popliteal and inguinal LNs, anaesthetized C57BL/6 mice were first injected with 50 µl anti-
483 LYVE1-Alexa Fluor 488 antibody (20 µg/ml, R&D Systems) into the rear right hock, an
484 alternative injection site to the footpad which is less invasive while allowing strong
485 labelling (72). After 8 hours, 50 µl WGA-Alexa Fluor 647 (1 mg/ml, Invitrogen) were injected
486 in the same site and after a circulation period of 1 hour, the blood system of the whole body
487 was labelled by injecting 100 µl of WGA-Alexa Fluor 555 (5 mg/ml, Invitrogen) with 10 µl
488 Heparin (100 units/ml) into the tail vein or vena cava of the anaesthetized mouse for a duration
489 2 minutes. Freshly excised murine tissue was fixed in 4% PFA, 3% sucrose at 4°C overnight
490 and embedded in LR white resin (medium grade, ProSciTech) for confocal imaging as
491 described above. Standard confocal microscopy was performed using a Leica TCS SP2
492 equipped with a Leica HCX APO L 40.0x0.80 W UV water objective (Leica microsystems) at
493 a voxel resolution of 0.36 x 0.36 x 1 µm.

494 **Immunohistochemistry**

495 Freshly excised popliteal or inguinal LNs were snap frozen in O.C.T. compound (Sakura
496 Finetek) and sectioned into 7 µm thick tissue sections. A protocol for multicolor
497 immunohistochemistry established by Lloyd et al. (73) was adopted for immunostaining using
498 up to four labels. These include antibodies against LYVE-1 (R&D Systems, clone 223322),

499 collagen I (Abcam), laminin (Abcam), CD21/CD35-Biotin (Biolegend, clone 7E9), Ki-67
500 (Biolegend, clone 16A8), CD3e (BD Pharmingen, clone 500A2), and CD45R/B220 (BD
501 Pharmingen, clone RA3-6B2). Primary antibodies were detected with Alexa Fluor 488, 555,
502 or 647 conjugated goat secondary antibodies or Streptavidin (Invitrogen) and nuclei labelled
503 with DAPI (Invitrogen). Stained immunohistochemistry sections were mounted using ProLong
504 Gold Antifade reagent (Invitrogen) and photographed on a Nikon Eclipse Ni-U epifluorescence
505 microscope (Nikon Instruments) using a SPOT Pursuit 1.4MP monochrome camera (Scitech).
506 Acquired images were pseudo-colored, processed, and superimposed employing the
507 Cytosketch software (Cytocode Limited).

508 **EVIS imaging and image processing**

509 Extended-volume confocal imaging (EVIS) is a confocal block-face imaging method that can
510 capture large 3D regions of fluorescently labelled tissue up to several millimeters thick at a
511 pixel resolution of up to 0.5 μm . In an iterative process, a resin-embedded sample is moved
512 between a confocal laser scanning microscope (TCS 4D CLSM, Leica) and a precision miller
513 (Leica SP2600 ultramill, Leica) both mounted on a high-precision three-axis translation stage
514 (Aerotech, US) and controlled by imaging software written in LabVIEWTM (National
515 Instruments), whereby previously imaged sections are removed in between imaging rounds as
516 previously described (33). Image acquisition was performed using an Omnicrome
517 krypton/argon laser (Melles Griot) for sample illumination, a 20x water immersion lens (HC
518 PL APO, 0.70 NA, Leica), 4x line averaging, and an image overlap of 50%. Individual 8-bit
519 (grayscale) images acquired at '1 μm pixel resolution' contained 512 x 512 pixels covering an
520 area of 500 x 500 μm , providing a pixel resolution of 0.98 μm . By acquiring successive images
521 at a z-spacing of 1 μm , an isotropic voxel size of (1 μm)³ was achieved. Precise xyz-registration
522 of the acquired image stack in conjunction with custom-designed image processing and

523 assembly software (LabVIEW™, (33, 34)) enables the composition of seamless 3D images.
524 As part of this process, individual images underwent background correction, deconvolution,
525 and denoising, before being merged into x-y mosaics and assembled into a 3D volume image.
526 To further improve the quality of the generated 3D images and reduce the fluctuation of signal
527 intensities between individual z planes across the 3D image stack, we employed an equalization
528 algorithm to adjust the average image intensity in z direction. Rather than having a fixed target
529 for correction, a variable (‘smoothed’) ideal intensity was used for each z plane, to account for
530 the changing diameter across the spherical LN sample. Using the formula below, a correction
531 factor $f(z)$ was obtained for each z plane and multiplied with the pixel intensities on the
532 respective plane to create an equalized image. The corrected 3D image displayed a significantly
533 reduced intensity variation and was better suited for image analysis.

$$534 f(z) = a * \frac{SA(z)}{A(z)} + (1 - a)$$

535

536 $f(z)$ = correction factor for each z plane

537 A = average intensity (above a fixed threshold to eliminate noise)

538 SA = smoothed average intensity

539 $a = 0.9$ (to prevent over-correction)

540 **Network extraction and quantification**

541 *Conduit network extraction.* The voxel-based 3D EVIS image of LN conduits was processed
542 to extract a connected conduit network suitable for 3D measurements. This was performed
543 using a modified set of the tools we previously designed to isolate the blood vessel network
544 from fluorescent 3D images of a mesenteric LN (33). In short, the grayscale 3D image is

545 segmented using local thresholding, and the largest connected object selected to be
546 skeletonized, followed by applying a tracing algorithm that transforms information from the
547 segmented image and its skeleton into a topology map. This procedure generates a description
548 of the network as a collection of connected tube segments, together with additional files
549 allowing 3D visualization and manipulation. The image processing parameters were chosen
550 specifically to allow for capturing fine conduit channels within the TCZ, while medullary
551 regions with a high intensity of staining were excluded. To further narrow down the selection
552 of TCZ conduits, B cell regions near the surface of the LN were manually removed using the
553 filament editor in Amira (Thermo Fisher Scientific).

554 *Exclusion of blood vessel surrounding conduit sleeves.* One feature of the conduit network
555 inevitably created a challenge for the processing: large blood vessels are often completely
556 surrounded by conduits, resulting in the formation of conduit sleeves, hollow tubes which
557 cannot be reduced to a single centerline by the skeletonization algorithm (S3 Fig). Previous
558 studies have manually excluded these parts of the network (30), but given the large size of the
559 present network we required a more automated approach in order to omit these sleeves. To this
560 end we utilized the blood vessel image data from the same specimen, optimized using our
561 previously described tools (33). We added them to the segmented image of the conduits, and
562 filled remaining gaps manually and by using the segmentation tool in Amira, to obtain a
563 combined 3D image of the conduits and blood vessels. As a result, conduits paths surrounding
564 large blood vessels are reduced to the core blood vessel path helping to avoid artifacts and
565 preserving the continuity of the network. Alternatively, the segmented image of the blood
566 vasculature was subjected to ‘region growing’ in Amira and subtracted from the segmented
567 image of the conduits, using a homemade tool that allows the addition and subtraction of pixel
568 values between two images at the same location, in order to obtain a largely ‘blood vessel free’
569 conduit image. Both conduit datasets, either containing filled blood vessels or no blood vessels,

570 were subjected to network extraction and topology analysis separately. Depending on the
571 experimental question, we used either of these networks for the subsequent analysis as
572 described accordingly (Fig 2 d-f).

573 *Quantitative 3D measurements.* The network topology map obtained from the extraction allows
574 direct read-outs of network parameters, providing the number of segments, their volumes, the
575 number of vertices per branch point, the branching angles, and length measurements. We used
576 the blood vessel-free conduit topology map in this measurement, in order to obtain
577 representative values for the conduit network without the contribution of blood vessels. In the
578 calculation of branching angles, only segments with a length above 4 μm were chosen, to avoid
579 the jittering artefact cause by very short segments. Additional tools were utilized to calculate
580 the minimum distance from points in the network to the closest conduit (33), providing a
581 measure of spacing of neighboring segments and allowing the gaps between them to be
582 visualized as lit voxels. In this calculation all segments including potential blood vessels were
583 assessed to avoid creating artificial gaps.

584 In order to investigate the possibility that there was a ‘preferred’ orientation of conduit
585 segments in the network, a method was developed to estimate the tendency of conduits to align
586 with a set of 13 directions roughly spanning the 3D range. The directions were chosen
587 corresponding to the lines connecting a point in a regular 3D grid to its 26 nearest neighbors.
588 The distribution of segment directions over these 13 reference directions was calculated by
589 summing the magnitude of segment projections onto the 13 lines, then normalizing. The results
590 were visualized in LabVIEW (National Instruments).

591 A ‘moving average’ display providing insight into the relative segment density was obtained
592 by first computing the averaged voxel densities of cubes with a set radius (e.g. 10 μm) while
593 moving in 2 μm steps across the binary volume image, then rescaling the density values from

594 0-1 to 0-255, and finally visualizing the resulting averaged 3D image as a greyscale or false-
595 colored (e.g. heatmap) image using ImageJ (2D) and Amira (3D).

596 *Selection of subregions.* To specifically measure and compare anatomical differences between
597 the outer and inner TCZs, spherical subregions with a diameter of 100 μm were selected for
598 individual analysis from both zones. Since the identification of non-touching subregions within
599 an irregular shaped 3D volume is not trivial and automated tools are lacking, we manually
600 selected the center points for each of the subregions based on the observable segment density
601 in z planes using ImageJ (NIH). By specifying a center point and radius in a 3D cropping tool,
602 these regions of interest could be isolated and their topology determined individually. As
603 above, the topology map exclusive of blood vessels was used to obtain conduit-specific
604 parameters but blood vessels were included to estimate the distance distribution to the nearest
605 conduit.

606 *Modelling T cell motility.* Based on the current understanding that the FRC network provides
607 a substrate for T cell migration, we sought to simulate T cell motility on the 3D conduit
608 network. The coefficient of motility, C_m , which is analogous to a diffusion coefficient (74),
609 was estimated by simulating the movement of a large number of cells on the network, subject
610 to certain assumptions about speed and behavior at junctions. The procedure is as follows. A
611 large number of cell paths through the network are simulated, the starting point (and starting
612 direction) of each path chosen at random. Each cell is initially assigned a speed drawn from a
613 Gaussian distribution with specified mean (here: 13 $\mu\text{m min}^{-1}$) and coefficient of variation -
614 (standard deviation)/mean (here: 0.1). The cell moves with this constant speed along the
615 network segments. When a segment junction is encountered the branch taken by the cell is
616 determined randomly, according to the following procedure. For each possible branch, k , the
617 turning angle θ is determined, and for an angle less than 90° the probability weight $w(k)$
618 associated with that branch is computed as $\cos^4(\theta)$, the fourth power of the cosine of the turning

619 angle, otherwise $w(k)$ is set to a very small value (0.001). The probability of taking branch k is
620 then given by $w(k)$ divided by the sum of all the weights. The actual branch taken is then
621 determined in the usual way by generating a random variate with a uniform distribution. If a
622 cell reaches a dead-end in the network the direction of movement along the segment is reversed.
623 To reduce the encounter of dead-ends which could skew the observed C_m , each tested network
624 initially underwent a healing step of pruning and joining dead-ending segments to neighboring
625 vertices with a maximum branch length of 15 μm .

626 In short, if the junction-directed unit vector corresponding to the branch that the cell is on is
627 $v(0)$, and there are N_b branches the cell can take, with unit vectors $[v(k), k=1, \dots, N_b]$ directed away
628 from the junction, then the turning angle onto the k th branch is given by the dot-product of two
629 unit vectors (\cos^{-1} is the inverse cosine function.):

$$630 \theta(k) = \cos^{-1}(v(0) \cdot v(k))$$

631 Then the probability of taking branch k is given by:

$$632 P(k) = \frac{w(k)}{\sum_{j=1}^{j=N_b} w(j)}$$

$$633 w(k) = (\cos(\theta(k)))^4 \quad \text{if } \cos(\theta(k)) > 0$$

$$634 \quad = 0.001 \text{ otherwise}$$

635

636 The movement of each of 5000 cells across the network was simulated in this way for a period
637 of one hour. In order to avoid the possibility of a cell reaching the boundary of the network the
638 starting points were restricted to those falling within a sphere of radius 100 μm centered at the
639 center of the LN, unless otherwise specified for TCZ subregions. The average squared distance

640 of cells from their start points was computed at 5 min intervals, and plotted. The estimate of
641 the coefficient of motility (C_m) is the slope of the resulting line divided by 6. Since the curve
642 is not a straight line the average slope was estimated from the points at times 0 and 60 min (=
643 T).

644 Let $(x_i(t), y_i(t), z_i(t))$ be the position of cell i at time t , N = number of cell paths simulated.

$$645 C_m = \frac{\sum_{i=1}^N \left\{ (x_i(T) - x_i(0))^2 + (y_i(T) - y_i(0))^2 + (z_i(T) - z_i(0))^2 \right\}}{6TN}$$

646 To account for the tissue shrinkage that occurs during the embedding process (estimated to be
647 20% in each direction), a correction factor of 1.25 can be applied to all segment lengths in this
648 simulation.

649 A selection of 20 tracks, normalized to the same starting point, was visualized in a spider plot
650 using CMGUI. Calculation of C_m was performed on the conduit network in which blood vessels
651 were removed and on the full network including blood vessels, to account for the possibility
652 that blood vessels can serve as additional migration paths.

653

654 *Visualization.* 3D images obtained from extended-volume or conventional confocal imaging
655 were acquired as greyscale 3D tiff files in raw format and were pseudo-colored, processed, and
656 superimposed with the 3D rendering programs Voxx , ImageJ (NIH), Amira (Thermo Fisher
657 Scientific), or Imaris (Bitplane). Visualization of 3D image data was performed by generating
658 2D projections of rendered volume images, isolating and displaying single z-planes, or by
659 accumulating several z planes over a range of 10-20 μm to provide ‘thick volume sections’ that
660 can allow better insight into the arrangement of fine structures over a restricted range of tissue.
661 Selected programs such as Voxx and Imaris further allowed the generation of high quality

662 movie files. The 3D rendering software CMGUI was employed for rendering the network and
663 the simulated cell paths. Graphs were generated in GraphPad Prism version 7.02 for Windows
664 (GraphPad Software).

665 **Quantification and Statistical Analysis**

666 All statistical analysis was performed in GraphPad Prism v7.03. Statistical parameters
667 including the exact value of N, the definition of center, dispersion and precision measures
668 (mean \pm SD) and statistical significance are reported in the Fig 3 and the respective figure
669 legend. Data is judged to be statistically significant when $p < 0.05$ by two-tailed Student's t
670 test. In figures, asterisks denote statistical significance as calculated by Student's t test (*, $p <$
671 0.05 ; **, $p < 0.01$; ***, $p < 0.001$; ****, $p < 0.0001$; ns = not significant).

672 **Data and Code Availability**

673 A custom-written toolset to extract volumetric network information from a voxel-based 3D
674 image was modified from our previous work (33) to allow for the isolation of a connected
675 conduit network in the T cell zone. The source code for these tools can be found under:
676 <https://github.com/gibbogle/vessel-tools.git> . The 3D data presented in this study are available
677 from the corresponding author upon reasonable request.

678 **Acknowledgments**

679 The authors gratefully acknowledge the help and advice of Dr Adrian Turner, Mrs Amorita
680 Petzer, Ms Shorena Nachkebia, and the members of the Dunbar and LeGrice laboratories at the
681 University of Auckland. We thank the Biomedical Imaging Research Unit (BIRU) at the
682 University of Auckland for providing access to the image processing software Amira. G.B.
683 acknowledges the support of the Auckland Bioengineering Institute. This work was partially
684 funded by the Maurice Wilkins Centre, a national Centre of Research Excellence hosted by the
685 University of Auckland.

686 **Author Contributions**

687 P.R.D., I.D.K. and G.B. conceived and designed the study. I.D.K. conducted the experiments
688 and analyzed the data. A.P. supervised the surgical experiments. G.B.S. supervised the EVIS
689 imaging and image processing, and developed targeted tools to assist the image processing.
690 G.B. developed computational tools and supervised the analysis. I.D.K., G.B. and P.R.D. wrote
691 the manuscript. G.B.S., A.P. and I.J.L. gave technical support and conceptual advice on the
692 project.

693 **Competing Interests**

694 The authors declare no competing financial interests.

695 References

- 696 1. Junt T, Scandella E, Ludewig B. Form follows function: lymphoid tissue
697 microarchitecture in antimicrobial immune defence. *Nat Rev Immunol.*
698 2008;8(10):764-75.
- 699 2. Mueller SN, Germain RN. Stromal cell contributions to the homeostasis and
700 functionality of the immune system. *Nat Rev Immunol.* 2009;9(9):618-29.
- 701 3. von Andrian UH, Mempel TR. Homing and cellular traffic in lymph nodes. *Nat*
702 *Rev Immunol.* 2003;3(11):867-78.
- 703 4. Anderson AO, Anderson ND. Studies on the structure and permeability of the
704 microvasculature in normal rat lymph nodes. *Am J Pathol.* 1975;80(3):387-418.
- 705 5. Gretz JE, Anderson AO, Shaw S. Cords, channels, corridors and conduits:
706 critical architectural elements facilitating cell interactions in the lymph node cortex.
707 *Immunol Rev.* 1997;156:11-24.
- 708 6. Brown FD, Turley SJ. Fibroblastic reticular cells: organization and regulation
709 of the T lymphocyte life cycle. *J Immunol.* 2015;194(4):1389-94.
- 710 7. Fletcher AL, Acton SE, Knoblich K. Lymph node fibroblastic reticular cells in
711 health and disease. *Nat Rev Immunol.* 2015;15(6):350-61.
- 712 8. Girard JP, Moussion C, Forster R. HEVs, lymphatics and homeostatic immune
713 cell trafficking in lymph nodes. *Nat Rev Immunol.* 2012;12(11):762-73.
- 714 9. Forster R, Schubel A, Breitfeld D, Kremmer E, Renner-Muller I, Wolf E, et al.
715 CCR7 coordinates the primary immune response by establishing functional
716 microenvironments in secondary lymphoid organs. *Cell.* 1999;99(1):23-33.
- 717 10. Cremasco V, Woodruff MC, Onder L, Cupovic J, Nieves-Bonilla JM,
718 Schildberg FA, et al. B cell homeostasis and follicle confines are governed by
719 fibroblastic reticular cells. *Nat Immunol.* 2014;15(10):973-81.
- 720 11. Malhotra D, Fletcher AL, Astarita J, Lukacs-Kornek V, Tayalia P, Gonzalez
721 SF, et al. Transcriptional profiling of stroma from inflamed and resting lymph nodes
722 defines immunological hallmarks. *Nat Immunol.* 2012;13(5):499-510.
- 723 12. Astarita JL, Cremasco V, Fu J, Darnell MC, Peck JR, Nieves-Bonilla JM, et al.
724 The CLEC-2-podoplanin axis controls the contractility of fibroblastic reticular cells and
725 lymph node microarchitecture. *Nat Immunol.* 2015;16(1):75-84.
- 726 13. Acton SE, Farrugia AJ, Astarita JL, Mourao-Sa D, Jenkins RP, Nye E, et al.
727 Dendritic cells control fibroblastic reticular network tension and lymph node
728 expansion. *Nature.* 2014;514(7523):498-502.
- 729 14. Scandella E, Bolinger B, Lattmann E, Miller S, Favre S, Littman DR, et al.
730 Restoration of lymphoid organ integrity through the interaction of lymphoid tissue-
731 inducer cells with stroma of the T cell zone. *Nat Immunol.* 2008;9(6):667-75.

- 732 15. Link A, Hardie DL, Favre S, Britschgi MR, Adams DH, Sixt M, et al.
733 Association of T-zone reticular networks and conduits with ectopic lymphoid tissues in
734 mice and humans. *Am J Pathol.* 2011;178(4):1662-75.
- 735 16. Stranford S, Ruddle NH. Follicular dendritic cells, conduits, lymphatic vessels,
736 and high endothelial venules in tertiary lymphoid organs: Parallels with lymph node
737 stroma. *Front Immunol.* 2012;3:350.
- 738 17. Roozendaal R, Mebius RE, Kraal G. The conduit system of the lymph node. *Int*
739 *Immunol.* 2008;20(12):1483-7.
- 740 18. Gretz JE, Norbury CC, Anderson AO, Proudfoot AE, Shaw S. Lymph-borne
741 chemokines and other low molecular weight molecules reach high endothelial venules
742 via specialized conduits while a functional barrier limits access to the lymphocyte
743 microenvironments in lymph node cortex. *J Exp Med.* 2000;192(10):1425-40.
- 744 19. Sixt M, Kanazawa N, Selg M, Samson T, Roos G, Reinhardt DP, et al. The
745 conduit system transports soluble antigens from the afferent lymph to resident dendritic
746 cells in the T cell area of the lymph node. *Immunity.* 2005;22(1):19-29.
- 747 20. Rantakari P, Auvinen K, Jappinen N, Kapraali M, Valtonen J, Karikoski M, et
748 al. The endothelial protein PLVAP in lymphatics controls the entry of lymphocytes and
749 antigens into lymph nodes. *Nat Immunol.* 2015;16(4):386-96.
- 750 21. Anderson AO, Shaw S. T cell adhesion to endothelium: the FRC conduit system
751 and other anatomic and molecular features which facilitate the adhesion cascade in
752 lymph node. *Semin Immunol.* 1993;5(4):271-82.
- 753 22. Palframan RT, Jung S, Cheng G, Weninger W, Luo Y, Dorf M, et al.
754 Inflammatory chemokine transport and presentation in HEV: a remote control
755 mechanism for monocyte recruitment to lymph nodes in inflamed tissues. *J Exp Med.*
756 2001;194(9):1361-73.
- 757 23. Stein JV, Rot A, Luo Y, Narasimhaswamy M, Nakano H, Gunn MD, et al. The
758 CC chemokine thymus-derived chemotactic agent 4 (TCA-4, secondary lymphoid
759 tissue chemokine, 6CKine, exodus-2) triggers lymphocyte function-associated antigen
760 1-mediated arrest of rolling T lymphocytes in peripheral lymph node high endothelial
761 venules. *J Exp Med.* 2000;191(1):61-76.
- 762 24. Bajenoff M. Stromal cells control soluble material and cellular transport in
763 lymph nodes. *Front Immunol.* 2012;3:304.
- 764 25. Textor J, Mandl JN, de Boer RJ. The Reticular Cell Network: A Robust
765 Backbone for Immune Responses. *PLoS Biol.* 2016;14(10):e2000827.
- 766 26. Beltman JB, Maree AF, Lynch JN, Miller MJ, de Boer RJ. Lymph node
767 topology dictates T cell migration behavior. *J Exp Med.* 2007;204(4):771-80.
- 768 27. Graw F, Regoes RR. Influence of the fibroblastic reticular network on cell-cell
769 interactions in lymphoid organs. *PLoS Comput Biol.* 2012;8(3):e1002436.

- 770 28. Donovan GM, Lythe G. T-cell movement on the reticular network. *J Theor Biol.*
771 2012;295:59-67.
- 772 29. Savinkov R, Kislitsyn A, Watson DJ, Loon Rv, Sazonov I, Novkovic M, et al.
773 Data-driven modelling of the FRC network for studying the fluid flow in the conduit
774 system. *Eng Appl Artif Intell.* 2017;62:341-9.
- 775 30. Novkovic M, Onder L, Cupovic J, Abe J, Bomze D, Cremasco V, et al.
776 Topological Small-World Organization of the Fibroblastic Reticular Cell Network
777 Determines Lymph Node Functionality. *PLoS Biol.* 2016;14(7):e1002515.
- 778 31. Ntziachristos V. Going deeper than microscopy: the optical imaging frontier in
779 biology. *Nat Methods.* 2010;7(8):603-14.
- 780 32. Mayer J, Swoger J, Ozga AJ, Stein JV, Sharpe J. Quantitative measurements in
781 3-dimensional datasets of mouse lymph nodes resolve organ-wide functional
782 dependencies. *Comput Math Methods Med.* 2012;2012:128431.
- 783 33. Kelch ID, Bogle G, Sands GB, Phillips AR, LeGrice IJ, Dunbar PR. Organ-
784 wide 3D-imaging and topological analysis of the continuous microvascular network in
785 a murine lymph node. *Sci Rep.* 2015;5:16534.
- 786 34. Sands GB, Gerneke DA, Hooks DA, Green CR, Smaill BH, LeGrice IJ.
787 Automated imaging of extended tissue volumes using confocal microscopy. *Microsc*
788 *Res Tech.* 2005;67(5):227-39.
- 789 35. Ludewig B, Stein JV, Sharpe J, Cervantes-Barragan L, Thiel V, Bocharov G. A
790 global "imaging" view on systems approaches in immunology. *Eur J Immunol.*
791 2012;42(12):3116-25.
- 792 36. Willard-Mack CL. Normal structure, function, and histology of lymph nodes.
793 *Toxicol Pathol.* 2006;34(5):409-24.
- 794 37. Katakai T, Hara T, Lee JH, Gonda H, Sugai M, Shimizu A. A novel reticular
795 stromal structure in lymph node cortex: an immuno-platform for interactions among
796 dendritic cells, T cells and B cells. *Int Immunol.* 2004;16(8):1133-42.
- 797 38. Cyster JG, Schwab SR. Sphingosine-1-phosphate and lymphocyte egress from
798 lymphoid organs. *Annu Rev Immunol.* 2012;30:69-94.
- 799 39. Gonzalez SF, Degn SE, Pitcher LA, Woodruff M, Heesters BA, Carroll MC.
800 Trafficking of B cell antigen in lymph nodes. *Annu Rev Immunol.* 2011;29:215-33.
- 801 40. Miller MJ, Wei SH, Parker I, Cahalan MD. Two-photon imaging of lymphocyte
802 motility and antigen response in intact lymph node. *Science.* 2002;296(5574):1869-73.
- 803 41. Worbs T, Mempel TR, Bolter J, von Andrian UH, Forster R. CCR7 ligands
804 stimulate the intranodal motility of T lymphocytes in vivo. *J Exp Med.*
805 2007;204(3):489-95.

- 806 42. Nombela-Arrieta C, Mempel TR, Soriano SF, Mazo I, Wymann MP, Hirsch E,
807 et al. A central role for DOCK2 during interstitial lymphocyte motility and sphingosine-
808 1-phosphate-mediated egress. *J Exp Med*. 2007;204(3):497-510.
- 809 43. Hons M, Kopf A, Hauschild R, Leithner A, Gaertner F, Abe J, et al. Chemokines
810 and integrins independently tune actin flow and substrate friction during intranodal
811 migration of T cells. *Nat Immunol*. 2018;19(6):606-16.
- 812 44. Mempel TR, Henrickson SE, Von Andrian UH. T-cell priming by dendritic cells
813 in lymph nodes occurs in three distinct phases. *Nature*. 2004;427(6970):154-9.
- 814 45. Majstoravich S, Zhang J, Nicholson-Dykstra S, Linder S, Friedrich W,
815 Siminovitch KA, et al. Lymphocyte microvilli are dynamic, actin-dependent structures
816 that do not require Wiskott-Aldrich syndrome protein (WASp) for their morphology.
817 *Blood*. 2004;104(5):1396-403.
- 818 46. Baekkevold ES, Yamanaka T, Palframan RT, Carlsen HS, Reinholt FP, von
819 Andrian UH, et al. The CCR7 ligand *elc* (CCL19) is transcytosed in high endothelial
820 venules and mediates T cell recruitment. *J Exp Med*. 2001;193(9):1105-12.
- 821 47. Grigorova IL, Panteleev M, Cyster JG. Lymph node cortical sinus organization
822 and relationship to lymphocyte egress dynamics and antigen exposure. *Proc Natl Acad
823 Sci USA*. 2010;107(47):20447-52.
- 824 48. Forster R, Braun A, Worbs T. Lymph node homing of T cells and dendritic cells
825 via afferent lymphatics. *Trends Immunol*. 2012;33(6):271-80.
- 826 49. Cavanagh LL, Weninger W. Dendritic cell behaviour in vivo: lessons learned
827 from intravital two-photon microscopy. *Immunol Cell Biol*. 2008;86(5):428-38.
- 828 50. Gerner MY, Casey KA, Kastenmuller W, Germain RN. Dendritic cell and
829 antigen dispersal landscapes regulate T cell immunity. *J Exp Med*. 2017;214(10):3105-
830 22.
- 831 51. Hickman HD, Takeda K, Skon CN, Murray FR, Hensley SE, Loomis J, et al.
832 Direct priming of antiviral CD8⁺ T cells in the peripheral interfollicular region of
833 lymph nodes. *Nat Immunol*. 2008;9(2):155-65.
- 834 52. Woodruff MC, Heesters BA, Herndon CN, Groom JR, Thomas PG, Luster AD,
835 et al. Trans-nodal migration of resident dendritic cells into medullary interfollicular
836 regions initiates immunity to influenza vaccine. *J Exp Med*. 2014;211(8):1611-21.
- 837 53. Kastenmuller W, Torabi-Parizi P, Subramanian N, Lammermann T, Germain
838 RN. A spatially-organized multicellular innate immune response in lymph nodes limits
839 systemic pathogen spread. *Cell*. 2012;150(6):1235-48.
- 840 54. Kastenmuller W, Brandes M, Wang Z, Herz J, Egen JG, Germain RN.
841 Peripheral prepositioning and local CXCL9 chemokine-mediated guidance orchestrate
842 rapid memory CD8⁺ T cell responses in the lymph node. *Immunity*. 2013;38(3):502-
843 13.

- 844 55. Gerner Michael Y, Kastenmuller W, Ifrim I, Kabat J, Germain Ronald N. Histo-
845 Cytometry: A Method for Highly Multiplex Quantitative Tissue Imaging Analysis
846 Applied to Dendritic Cell Subset Microanatomy in Lymph Nodes. *Immunity*.
847 2012;37(2):364-76.
- 848 56. Groom JR. Moving to the suburbs: T-cell positioning within lymph nodes
849 during activation and memory. *Immunol Cell Biol*. 2015;93(4):330-6.
- 850 57. Lian J, Luster AD. Chemokine-guided cell positioning in the lymph node
851 orchestrates the generation of adaptive immune responses. *Curr Opin Cell Biol*.
852 2015;36:1-6.
- 853 58. Gerner MY, Torabi-Parizi P, Germain RN. Strategically localized dendritic
854 cells promote rapid T cell responses to lymph-borne particulate antigens. *Immunity*.
855 2015;42(1):172-85.
- 856 59. Hara T, Shitara S, Imai K, Miyachi H, Kitano S, Yao H, et al. Identification of
857 IL-7-producing cells in primary and secondary lymphoid organs using IL-7-GFP
858 knock-in mice. *J Immunol*. 2012;189(4):1577-84.
- 859 60. Bajenoff M, Egen JG, Koo LY, Laugier JP, Brau F, Glaichenhaus N, et al.
860 Stromal cell networks regulate lymphocyte entry, migration, and territoriality in lymph
861 nodes. *Immunity*. 2006;25(6):989-1001.
- 862 61. Katakai T, Kinashi T. Microenvironmental Control of High-Speed Interstitial T
863 Cell Migration in the Lymph Node. *Front Immunol*. 2016;7:194.
- 864 62. Huang AY, Qi H, Germain RN. Illuminating the landscape of in vivo immunity:
865 insights from dynamic in situ imaging of secondary lymphoid tissues. *Immunity*.
866 2004;21(3):331-9.
- 867 63. Castellino F, Huang AY, Altan-Bonnet G, Stoll S, Scheinecker C, Germain RN.
868 Chemokines enhance immunity by guiding naive CD8+ T cells to sites of CD4+ T cell-
869 dendritic cell interaction. *Nature*. 2006;440(7086):890-5.
- 870 64. Bogle G, Dunbar PR. Simulating T-cell motility in the lymph node paracortex
871 with a packed lattice geometry. *Immunol Cell Biol*. 2008;86(8):676-87.
- 872 65. Cyster JG. B cell follicles and antigen encounters of the third kind. *Nat*
873 *Immunol*. 2010;11(11):989-96.
- 874 66. Bajenoff M, Germain RN. B-cell follicle development remodels the conduit
875 system and allows soluble antigen delivery to follicular dendritic cells. *Blood*.
876 2009;114(24):4989-97.
- 877 67. Roozendaal R, Mempel TR, Pitcher LA, Gonzalez SF, Verschoor A, Mebius
878 RE, et al. Conduits mediate transport of low-molecular-weight antigen to lymph node
879 follicles. *Immunity*. 2009;30(2):264-76.
- 880 68. Gonzalez SF, Kuligowski MP, Pitcher LA, Roozendaal R, Carroll MC. The role
881 of innate immunity in B cell acquisition of antigen within LNs. *Adv Immunol*.
882 2010;106:1-19.

- 883 69. Itano AA, McSorley SJ, Reinhardt RL, Ehst BD, Ingulli E, Rudensky AY, et al.
884 Distinct Dendritic Cell Populations Sequentially Present Antigen to CD4 T Cells and
885 Stimulate Different Aspects of Cell-Mediated Immunity. *Immunity*. 2003;19(1):47-57.
- 886 70. Thierry GR, Kuka M, De Giovanni M, Mondor I, Brouilly N, Iannacone M, et
887 al. The conduit system exports locally secreted IgM from lymph nodes. *J Exp Med*.
888 2018.
- 889 71. Moyer TJ, Zmolek AC, Irvine DJ. Beyond antigens and adjuvants: formulating
890 future vaccines. *J Clin Invest*. 2016;126(3):799-808.
- 891 72. Kamala T. Hock immunization: a humane alternative to mouse footpad
892 injections. *J Immunol Methods*. 2007;328(1-2):204-14.
- 893 73. Lloyd CM, Phillips AR, Cooper GJ, Dunbar PR. Three-colour fluorescence
894 immunohistochemistry reveals the diversity of cells staining for macrophage markers
895 in murine spleen and liver. *J Immunol Methods*. 2008;334(1-2):70-81.
- 896 74. Cahalan MD, Parker I. Choreography of cell motility and interaction dynamics
897 imaged by two-photon microscopy in lymphoid organs. *Annu Rev Immunol*.
898 2008;26:585-626.

899 Supplementary Items Titles

900 [S1-S5 Fig.](#)

901 [S1 Video](#). Fly-through animation of an entire murine LN captured by EVIS imaging. 3D image
902 reconstruction of this dataset visualizes the lymphatic (red glow) and blood (green)
903 passageways in a slice-by-slice view moving through z sections of 20 μm thickness and
904 provides an interior view of LN sub-compartments including the staining-rich medulla, a dense
905 mesh of conduit channels in the central TCZ, and the B cell follicles emerging near the SCS at
906 the rim of the LN. Image reconstruction and animation was performed in Voxx. Related to [Fig](#)
907 [1](#).

908 [S2 Video](#). This fly-through animation is moving slice-by-slice through the 3D volume image of
909 a murine LN in optical z sections of 20 μm thickness, zoomed into the interface between the
910 paracortex and the medulla. Blood vessels (green) penetrate through the LN volume rich in
911 lymphatic staining (red glow), each surrounded by a conduit sleeve. Conduit channels
912 frequently terminate on cortical sinuses continuous with the lymphatic system (sinuses) of the
913 medulla. The dataset was acquired using EVIS imaging and visualized in Voxx. Related to [Fig](#)
914 [1](#).

915 [S2 Video](#). 3D surface representation and animation of the LN blood vessels (red), lymphatic
916 sinuses (green), and conduit channels (grey). A crop from the edge of the paracortical region
917 of a WGA-perfused murine LN exemplifies the tight relationship of the blood and lymphatic
918 passageways within the LN as conduit channels meet a plexus of lymphatic sinuses. Several
919 blood vessels can be seen enclosed by a sleeve of conduits. The 3D image data were generated
920 using EVIS imaging, lymphatic sinuses were isolated from the conduit data with the help of

921 custom image processing tools, and surface rendering and animation of the data was performed
922 in Imaris. Related to [Fig 2](#).

923 [S4 Video](#). 3D reconstruction and animation of the blood vessel system (red) and lymphatic
924 channels (white) of a murine LN. In the first part of the animation the blood vasculature is
925 shown in full and rotated around the Y axis followed by a slice-by-slice view of the LN moving
926 through z sections of 10 μm thickness and displaying both the lymphatic and blood vessel
927 anatomy. Here, accumulations of the fluorescent tracer (WGA) used to visualize the lymphatic
928 passageways (white) can be observed within the B cell follicles, which appear as spherical
929 structures below the SCS devoid of an organized conduit network. Within these locations the
930 tracer material is labelling interconnected clusters resembling the FDC network. The 3D image
931 was acquired using EVIS imaging and reconstructed and animated in Imaris. Related to [Fig 4](#)
932 [a](#).

933 [S5 Video](#). A close-up view of a ‘follicular reservoir’ (white) within a B cell follicle labelled
934 with WGA within a murine LN. A 3D reconstructed image of the conduit system near the SCS
935 is reduced slice-by-slice to open the view to a spherical cluster with strong fluorescent label,
936 followed by building the image up again in a slice-by-slice manner. Standard confocal
937 microscopy was performed with a voxel resolution of 0.36 x 0.36 x 1 μm over a depth of 40
938 μm followed by image reconstruction and animation in Voxx. Related to [Fig 4 g, h](#).